CrossMark

The Effect of Fe, Co, and Ni Structural Promotion of Cryptomelane (KMn$_8$O$_{16}$) on the Catalytic Activity in Oxygen Evolution Reaction

Paweł Stelmachowski [1,2] · Alessandro H. A. Monteverde Videla [1] · Tomasz Jakubek [2] · Andrzej Kotarba [2] · Stefania Specchia [1]

Abstract

Transition metal (Fe, Co, Ni)-doped cryptomelane materials (K-OMS-2) were synthesized and characterized with the use of XRD, Raman spectroscopy, XPS, N$_2$-BET, H$_2$-TPR, and SEM. The electrocatalytic reactivity in oxygen evolution was evaluated with the use of the rotating disk electrode. It was found that the electrocatalytic activity is substantially enhanced for the cobalt-doped material, while iron and nickel doping have no, or even, negative effect on K-OMS-2. The structure of the material bulk is preserved in all cases, but the formation of additional birnessite phases can be evidenced for the iron and cobalt dopants. It is discussed that the reactivity enhancement of Co/K-OMS-2 can be related not only to the formation of cobalt-doped heterophases (cobaltane, birnessite) but also to the changes of the properties of pristine cryptomelane.

Keywords Manganese oxide · Catalyst · OER · Cryptomelane · K-OMS-2 · Electrocatalysis

Introduction

A sustainable production of H$_2$ as a chemical vector by a reliable and cost-effective way is one of the major challenges for the hydrogen economy. The electrolysis of water is a clean way to produce H$_2$ and O$_2$, without production of impurity by-product gasses. However, these reactions are not spontaneous at standard temperature and pressure, thus requiring the use of a catalyst and energy input to afford that purpose. From the rational point of view, electro-splitting of water is the only feasible option when electricity is obtained from non-conventional renewable energy sources, by utilizing as small as possible amounts of the electrical power [1]. The development of cheap catalysts, based on abundant materials, able to compete with noble metal based and expensive catalysts, such as RuO$_2$ or IrO$_2$, has been the focus for this application during the last years [2].

Current efforts are concentrated on the development of noble metal-free metal oxide and oxy-hydroxide-based catalysts [2–6]. Among them, perovskite-structure [7], spinel-structure [8, 9], and hydroxide-based [10, 11] materials are studied most intensively. Nickel-based materials exhibit the highest activity [12]. However, cobalt [13] and iron [6] containing materials can also be successfully optimized. Manganese oxides are gaining more and more interest as oxygen evolution electrocatalysts because of their proven high activity of biological photosynthesis [14]. Recently, several papers reported investigations of simple manganese oxides in acidic, neutral, or basic conditions [15–18]. Moreover, alkali nanostructured cryptomelane and birnessite materials were investigated with respect to possible enhancement of oxygen evolution activity by controlled introduction of potassium [19, 20], transition metals [21], and noble metals [22]. Although the reported activity is usually lower than that of nickel-based materials, the nature-provided examples of Mn-based compounds inspire new research directions for the optimization of Mn-based electrocatalysts.

✉ Paweł Stelmachowski
pawel.stelmachowski@uj.edu.pl

✉ Alessandro H. A. Monteverde Videla
alessandro.monteverdevidela@polito.it

[1] Department of Applied Science and Technology, Politecnico di Torino, Torino, Italy

[2] Faculty of Chemistry, Jagiellonian University in Kraków, Krakow, Poland

Cryptomelane is a nanoscale alkali-doped manganese octahedral molecular sieve (OMS). The high activity in oxidation reactions of Mn-based nanostructured materials is well known in heterogeneous catalysis [23–28]. Their high reactivity can be assigned to a combination of several features, such as beneficial porous structure, particular nanorod-type morphology, redox properties due to the mixed valence framework, and high oxygen mobility [29–32]. Cryptomelane is a hollandite type manganese oxide, with a tunneled structure (OMS-2) nanostructured by potassium (K-OMS-2). The tunnels are built up of four double-wide (2×2) slabs of octahedral MnO_6 units, connected by edges, forming tunnel dimensions of 4.6×4.6 Å [33]. Moreover, the introduction of heteroatoms in the structure of tunneled or layered oxides can bring about desired modification of their properties without changing their structure [34–36].

The possible activity enhancement of pristine cryptomelane was the motivation for the current study. The influence of the introduction of Fe, Co, and Ni structural promoters into the cryptomelane structure was investigated with respect to the oxygen evolution reaction.

Experimental

Material Preparation

Undoped cryptomelane (KMn_8O_{16}, K-OMS-2) was prepared by dissolving 11 g of manganese acetate in 40 ml of water, to which 5 ml of glacial acetic acid was added to adjust the pH. The solution was heated to boiling under reflux and maintained for 45 min. Potassium permanganate (6.5 g), dissolved in 150 ml of water, was then added. The mixture was stirred and heated for 24 h. The obtained solid phase was filtered and washed with distilled water until neutral pH, dried at 80 °C, and calcined at 450 °C for 2 h.

For the preparation of Co and Fe-substituted K-OMS-2 material ($KMn_{8-x}Co_xO_{16}$ and $KMn_{8-x}Fe_xO_{16}$), 0.01 mol of potassium nitrate was dissolved in 50 ml of distilled water along with a combined 0.0046 mol of manganese nitrate and the appropriately substituted metal nitrate in a 10:1 ratio. A cross-linking reagent, glucose, was dissolved in distilled water and added into the solution of salts. The molar ratio of salts and cross-linking reagent was adjusted to be 1:2. The mixture was stirred and heated to form a homogeneous clear sol. Then, the sol was evaporated and heated at 180 °C for 2 h in an electric oven. The resulting powder was calcined at 800 °C for 2 h in static air.

The nickel substituted K-OMS-2 material ($KMn_{8-x}Ni_xO_{16}$) was prepared by adding a 50-ml water solution containing nickel (0.663 g) and manganese (5.726 g) nitrates to 40 ml of potassium permanganate (2.768 g) mixed with 10 ml of acetic acid. Both solutions were previously heated and mixed with a temperature of ~ 60 °C. The mixtures were kept heated and mixed under a cooling condenser for 6 h. The formed precipitate was then filtered, washed with distilled water, and transferred to a crucible to be calcined at 400 °C for 2 h.

Physicochemical Characterization

The XRD patterns were recorded by a Rigaku MiniFlex powder diffractometer with Cu Kα radiation at 10 mA and 10 kV, 2θ step scans of 0.02°, and a counting time of 1 s per step. The micro-Raman spectra were recorded in ambient conditions using a Renishaw InVia spectrometer equipped with a Leica DMLM confocal microscope and a CCD detector, with an excitation wavelength of 785 nm. The laser power at the sample position was 1.5 mW (0.5% of total power) with a magnification of × 20. The Raman scattered light was collected in the spectral range of 200–850 cm^{-1}. At least six scans, 10 s each, were accumulated to ensure a sufficient signal to noise ratio.

Specific surface areas (SSA) were obtained by the three-point nitrogen adsorption method at liquid nitrogen temperatures using a Quantachrome Autosorb-1 automated gas sorption instrument. Samples were degassed at 120 °C under a flow of helium for 2 h before the analysis.

The relative ratio of metal ions was determined by using an energy-dispersive X-ray fluorescence (XRF) spectrometer (Thermo Scientific, ARL QUANT'X with the Rh anode, the X-rays of 4–50 kV). A 3.5-mm Si(Li) drifted crystal with a Peltier cooling (~ 185 K) was used as a detector. Quantitative analysis of the results was done semi-automatically with the use of UniQuant software, calibrated with a series of metallic standards.

X-ray photoelectron spectroscopy (XPS) was performed to determine the surface elemental composition of the catalysts. The analysis was carried out using a Thermo Fisher Scientific K-Alpha+ X-ray photoelectron spectrometer with monochromated Al Kα radiation operating at a power of 72 W (6 mA × 12 kV). A combination of low-energy electrons and argon ions were used to compensate charge. High-resolution scans were performed at a pass energy of 40 eV, while the survey spectra were acquired at a pass energy of 150 eV. Survey scans were recorded from 0 to 1350 eV. The high-resolution O 1s spectra were collected from 525 to 545 eV, C 1s from 279 to 305 eV, Mn 3s from 73 to 100 eV, Mn 2p from 632 to 660 eV, Fe 2p from 700 to 740 eV, and Co 2p from 771 to 812 eV. All the spectra were calibrated against a value of the C 1s binding energy of 284.8 eV. The procedure for the determination of an average Mn oxidation state is based on [37] and described in the Supplementary Information, p. 1.

SEM observations were carried out by TESCAN Vega 3 LUM electron microscope equipped with a LaB_6 cathode.

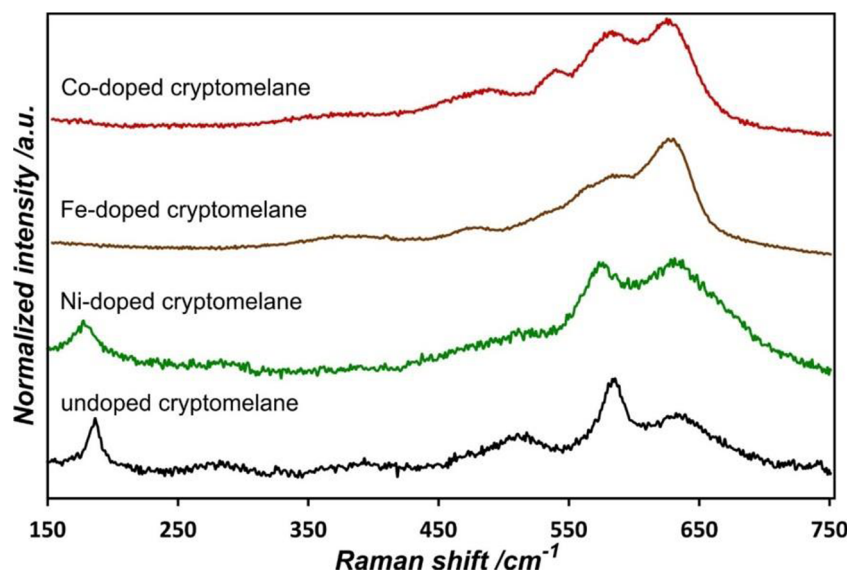Fig. 1 XRD patterns of the investigated cryptomelane-based catalysts
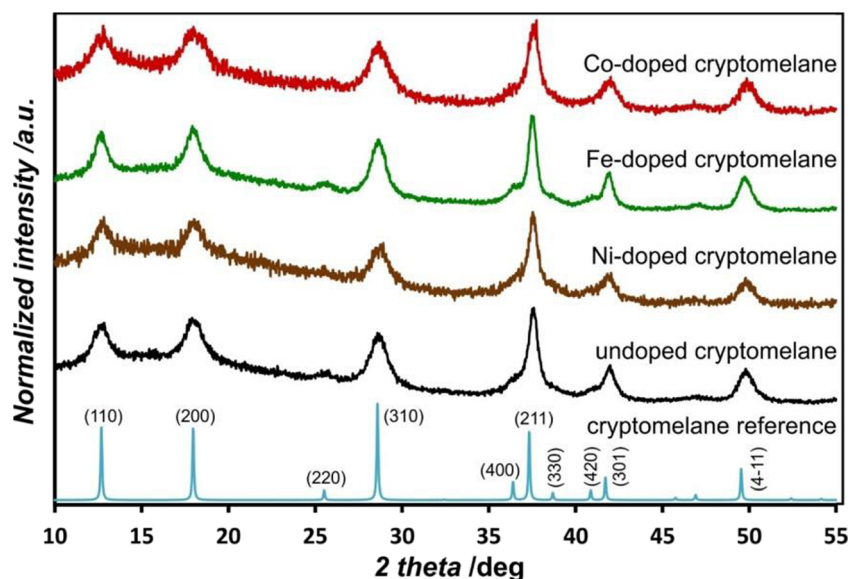
H_2-TPR measurements were obtained using a Chembet-300 apparatus with a TCD detector. About 0.025 g of sample was placed in an U-shaped quartz flow reactor (diameter ca. 5 mm) and kept in a helium stream for 1 h at 100 °C to remove adsorbed water. Next, the samples were cooled to ambient temperature and the TPR analysis was performed in the range of 25–600 °C, with a temperature ramp of 10 °C min^{-1} and a 30-cm^3 min^{-1} flow rate of reducing mixture (5% H_2 in Ar).

Electrocatalytic Activity

Reactivity in the oxygen evolution reaction (OER) of the investigated catalysts was evaluated using rotating disk electrode (RDE). All measurements were conducted using a Biologic S-150 instrument and a standard three-electrode electrochemical glass cell (Als-Japan). A Hg/HgO electrode and a gold wire were used as the reference and counter electrodes, respectively. After measurements, all potentials were converted to the reversible hydrogen electrode (RHE) scale. OER polarization curves were obtained at room temperature using steady-state staircase voltammetry testing in a nitrogen-saturated 0.1 M KOH. The electrode was rotated at 2000 rpm, and a step size of 10 mV and time period of 10 s step^{-1} was used. All tests were performed at room temperature. The counter was a spiral Gold wire with a length of 23 cm and diameter of 0.5 mm, with a total surface area of 3.6 cm^2 (Biologic Science Instruments, A-0.1263). A typical ink formulation was 20 mg of the catalyst powder, 210 µl of Nafion®, 600 µl of water, and 2400 µl of ethanol. The

Fig. 2 Raman spectra of the investigated cryptomelane-based catalysts

Fig. 3 SEM pictures of the investigated cryptomelane-based catalysts
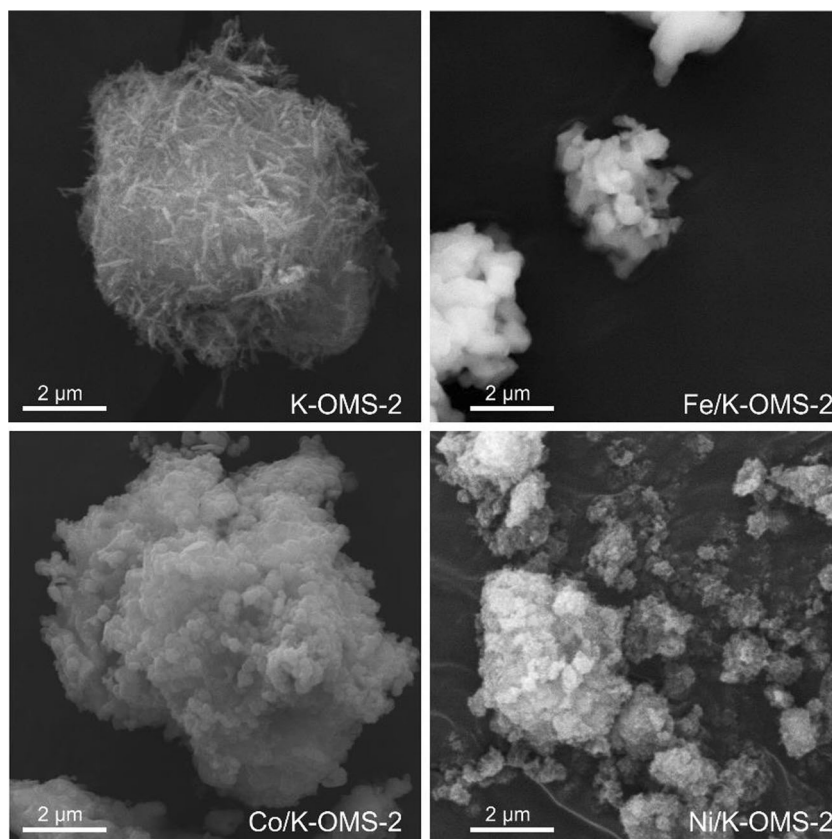
mixture was sonicated for 10 min, and 4 µl of the suspension was deposited on an electrode with an area of 0.125 cm^2.

Results and Discussion

The structural characterization performed with the use of X-ray diffractometer indicates that the bulk of the samples is composed of cryptomelane type materials (identified using the PDF database: 59159-ICSD), as shown in Fig. 1. All diffractograms feature broad peaks, which indicate small nanocrystal domains, for the investigated samples.

Raman spectra, which are more sensitive to the local coordination of metal cations and presence of heterophases, show that some structural changes occur for the Fe- and Co-doped samples, Fig. 2. Upon doping with Co and Fe, a partial change of the structure into the birnessite type takes place, as

indicated by an intensity increase of the high wavenumber peak and disappearance of the lowest wavenumber peak [38]. Unfortunately, the quantification of the cryptomelane and birnessite phases present in the samples is not feasible basing on the available XRD and Raman spectroscopy data. The nitrogen adsorption measurements indicate that for the Fe and Co-doped samples, SSA is lower by one and two orders of magnitude than for the undoped and Ni-doped samples: K-OMS-2 73 m^2 g^{-1}, Fe/K-OMS-2 10 m^2 g^{-1}, Co/K-OMS-2 ~ 1 m^2 g^{-1}, and Ni/K-OMS-2 120 m^2 g^{-1}. The changes of the crystals' morphology from cryptomelane nanorods [32] to flower-like birnessite material [39] may be the reason for the observed decrease. This interpretation is supported by the SEM pictures shown in Fig. 3, where the Co/K-OMS-2 and Fe/K-OMS-2 are visibly more compact, without the sharp features of the undoped cryptomelane.

The amounts of transition metals (TM) introduced into the K-OMS-2 structure vary considerably, being the highest for

Table 1 XRF analysis results of cryptomelane-based catalysts

Normalized composition	K-OMS-2	Fe/K-OMS-2	Co/K-OMS-2	Ni/K-OMS-2
K	0.07	0.29	0.24	0.03
Mn	1.00	1.00	1.00	1.00
Fe/Co/Ni	0.00	0.48	0.17	0.06

Table 2 XPS surface analysis results of cryptomelane-based catalysts

| Normalized composition	K-OMS-2	Fe/K-OMS-2	Co/K-OMS-2	Ni/K-OMS-2
K	0.16	0.60	0.58	0.05
Mn	1.00	1.00	1.00	1.00
O	1.97	3.32	2.47	1.55
Fe/Co/Ni	0.00	0.46	0.02	0.12
x in Mn^{x+}	3.56	3.75	3.85	3.32

Fe and the lowest for Ni. A general trend is that the more doping TM in the structure, the more potassium presence is also observed (Table 1).

Elemental analysis of the samples' surface was performed with the use of XPS. The elemental analysis with and without adventitious carbon is summarized in Tables S1 and S2 in the Supplementary Information. The high-resolution spectra for the regions of interest are collected in Figs. S1–S4 in the Supplementary Information. Table 2 summarizes the manganese normalized relative composition. In general, the relative cationic composition of the surface varies from sample to sample. The most striking observation is that the Ni-doped sample exhibits relatively low amount of oxygen. This indicates a reduced surface, with nickel in the form Ni^{2+}. Fe- and Co-doped samples, where the doping cations easily adopt multiple oxidation states, show higher surface oxygen content. The average manganese oxidation state is correlated with potassium content (Table 2; Fig. S5), which is reasonable from the crystal electronegativity point of view—the higher the relative content of low oxidation state K, the higher Mn oxidation state to compensate the oxygen negative charges. Relatively, low oxygen content in the Ni/K-OMS-2 sample

results in the reduction of the sample surface. A provisory charge balance analysis, comparing the sum of negatively and positively charged ions (Table S3), indicates that the positive charges exceed the sum of negative O^{2-} only for the Ni/K-OMS-2 sample. For the undoped cryptomelane, the surface is about neutral, while for the Co- and Fe-doped samples, the surface is oxidized.

The comparison of bulk composition of the cryptomelane materials determined with the XRF with the XPS results shows that in the case of the undoped and Fe- and Co-doped materials, the surface is enriched with potassium. Furthermore, it can be inferred that the surface content of Co in Co-doped cryptomelane is much lower than the bulk one.

Temperature-programmed reducibility tests with hydrogen, presented in Fig. 4, indicate that for the doped samples, the Co-doped one features reducibility similar to that of cryptomelane, which can be rationalized by the low Co content. On the other hand, the Fe- and Ni-doped samples show a decreased reducibility—the reduction peaks are shifted towards higher temperatures. The effect of iron doping can be rationalized by the observations that the presence of manganese retards the reduction of iron in mixed iron-manganese

Fig. 4 H_2-TPR profiles of the investigated cryptomelane-based catalysts
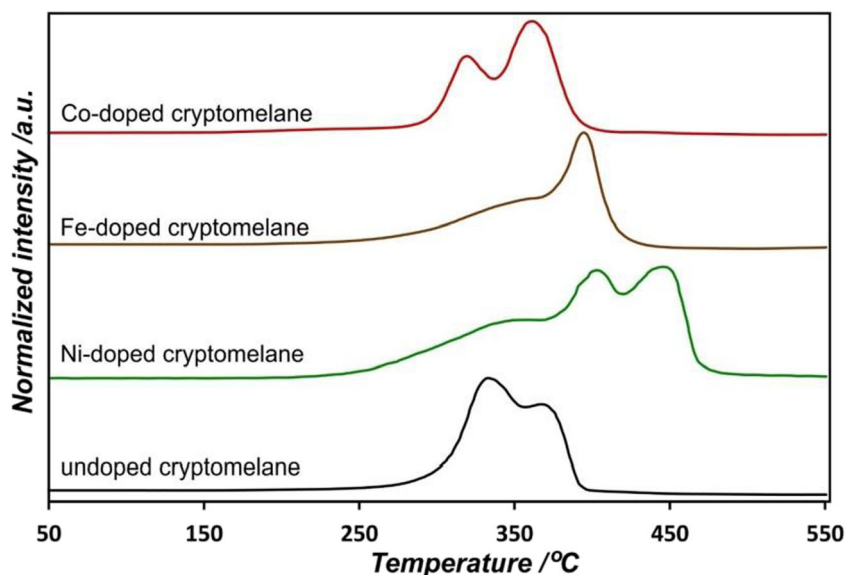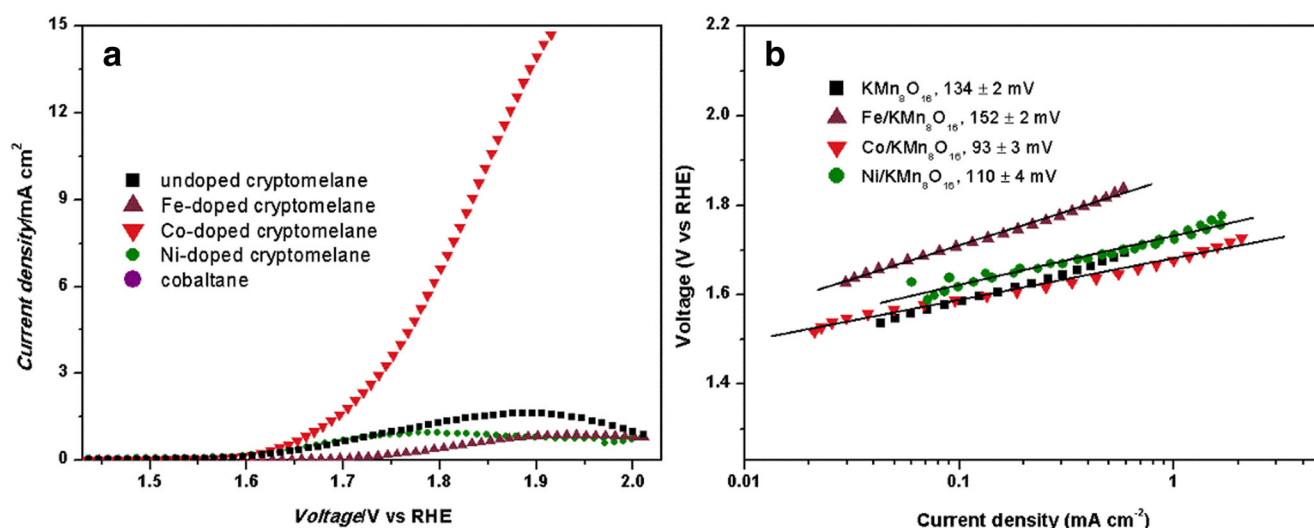
Fig. 5 **a** OER polarization curves and **b** Tafel plots of cryptomelane-based samples obtained at room temperature using steady-state staircase voltammetry, under nitrogen-saturated 0.1 M KOH

oxides [40]. The reduced state of the surface of Ni-doped sample can be responsible for the decreased reducibility of Ni/K-OMS-2.

Figure 5a shows the OER IR-corrected polarization curves of the synthesized catalysts under pseudo-steady state conditions in N_2-saturated 0.1 M KOH. Not surprisingly, undoped cryptomelane shows a negligible OER reactivity. However, doping the K-OMS-2 with Fe and Ni causes even further deterioration of the electrocatalytic activity. On the other hand, the addition of Co leads to a striking enhancement in oxygen evolution. The Tafel analysis of the polarization curves reveals that, indeed, Co/K-OMS-2 is characterized by the lowest slope value (Fig. 5b). The synthesized materials exhibit different Tafel slopes, KMn_8O_{16} (134 mV decade^{-1}), Fe/KMn_8O_{16} (152 mV decade^{-1}), Co/KMn_8O_{16} (93 mV decade^{-1}), and Ni/KMn_8O_{16} (116 mV decade^{-1}). Tafel slopes of about 120 mV decade^{-1} indicate the predominance of M-OH or M-O surface groups before the rate-determining step. When the surface adsorbed species produced in the early stage of the OER remains predominant, the Tafel slope decreases. The lower thermodynamic limits in the Butler-Volmer formalism predict Tafel slopes of 24, 40 ,or 60 mV decade^{-1}, which occur in the case of Ni, Co, and Ru surface oxides [1]. Specifically, for the case of Co/KMn_8O_{16} (93 mV decade^{-1}), the sample shows similar Tafel plot to Ir/cryptomelane-type sample (74 mV decade^{-1}) [22]. This comparison may suggest that using Ir or Co to form surface active species will be limited due to the chemistry of cryptomelane coordination, limiting activities with respect to pure oxides. However, the advantage of using doped cryptomelane materials is their stability at relevant reaction temperatures. The specific activity

(normalized by the specific surface area) and mass activity plots are presented in the Fig. S7A, B in the Supplementary Information. Since a similar mass of the catalyst was used for all the measurements, the mass activity plot is almost identical to the Fig. 5a. The specific activity plot in Fig. S7B amplifies the superior reactivity of the Co/cryptomelane sample due to its very low SSA.

The interesting characteristic of the Co/K-OMS-2 to bear in mind is that there is very little Co present in the material, especially on the surface (Table 2) and that the SSA of this material is very low. There are several possible interpretations of the reactivity enhancement upon cobalt doping. The formation of the active cobalt spinel, Co_3O_4, whose very good reactivity in OER is widely reported [9], can be excluded on the basis of the XRD and Raman spectroscopic results. The formation of birnessite type phase with intercalated Co was recently reported to improve oxygen evolution catalysis [21], and this could occur to some limited extent in the investigated sample. Furthermore, the formation of layered cobaltane phase, $K_{0.25}CoO_2$, can be responsible for the enhanced reactivity. Figure S6 in the Supplementary Information shows a comparison of such material with the Co/K-OMS-2 sample. Lastly, the increase of the OER activity can be due to the intrinsic activity of the Co-doped cryptomelane structure—not induced by the formation of other phases. For this material, the XPS results suggest the highest average oxidation state of manganese, in line with the proposed active centers for OER catalysts based on Mn, Ni, Co, and Ir [41]. H_2-TPR results show the highest lattice oxygen mobility

(reducibility) of the Co/K-OMS-2, which can also contribute to the reactivity enhancement. It is noteworthy that the Co/K-OMS-2 catalyst also shows the highest capacitance, in line with the observation that good supercapacitors are also good electrocatalysts (see cyclic voltammograms in Fig. S8). Interestingly, the stability of the Co-doped cryptomelane is very high and show very little or no degradation after 1000 polarization cycles, Fig. S6. Also, in the Fig. S6, a comparison with reference catalysts is presented (Ni/NiO, Co_3O_4, $NiCo_2O_4$) [42].

Conclusions

Fe-, Co-, and Ni-doped K-OMS-2 materials were successfully synthesized and characterized. The electrocatalytic reactivity in oxygen evolution is substantially enhanced for the cobalt-doped material. On the other hand, iron and nickel have no, or even, negative effect on the K-OMS-2 electrocatalytic activity. The possible negative effect can be related to the increased stability of the lattice oxygen, evidenced by the H_2-TPR. The structure of the material bulk is preserved in all cases, as evidenced by the X-ray diffractograms, but the formation of additional birnessite phases can be evidenced for the iron and cobalt dopants. It is shown that the reactivity enhancement of the Co/K-OMS-2 can be related not only to the formation of cobalt-doped heterophases (cobaltane, birnessite) but also to the induced modifications of the properties of pristine cryptomelane. The characteristic features of Co-doped K-OMS-2 are the low-temperature reducibility, with an increase of the average manganese oxidation state and an increased capacitance. The considerably better electrocatalytic activity of Co/K-OMS-2 is achieved despite disadvantageous very low Co content and negligible specific surface area.

References

1. R.L. Doyle, M.E.G. Lyons, in *The oxygen evolution reaction: mechanistic concepts and catalyst design*, ed. by S. Gimenez, J. Bisquert. Photoelectrochemical Solar Fuel Production: from Basic Principles to Advanced Devices (Springer, 2016), pp. 41–104. https://doi.org/10.1007/978-3-319-29641-8.

2. E. Fabbri, A. Habereder, K. Waltar, R. Kötz, T.J. Schmidt, R. Kotz, T.J. Schmidt, Developments and perspectives of oxide-based catalysts for the oxygen evolution reaction. Catal. Sci. Technol. **4**(11), 3800–3821 (2014). https://doi.org/10.1039/C4CY00669K

3. H.Y. Wang, Y.Y. Hsu, R. Chen, T.S. Chan, H.M. Chen, B. Liu, Ni^{3+}-induced formation of active NiOOH on the spinel Ni-Co oxide surface for efficient oxygen evolution reaction. Adv. Energy Mater. **5**(10), 1–8 (2015). https://doi.org/10.1002/aenm.201500091.

4. S. Zou, M.S. Burke, M.G. Kast, J. Fan, N. Danilovic, S.W. Boettcher, Fe (oxy)hydroxide oxygen evolution reaction electrocatalysis: intrinsic activity and the roles of electrical conductivity, substrate, and dissolution. Chem. Mater. **27**(23), 8011–8020 (2015). https://doi.org/10.1021/acs.chemmater.5b03404.

5. Y. Zhan, G. Du, S. Yang, C. Xu, M. Lu, Z. Liu, J.Y. Lee, Development of cobalt hydroxide as a bifunctional catalyst for oxygen electrocatalysis in alkaline solution. ACS Appl. Mater. Interfaces **7**(23), 12930–12936 (2015). https://doi.org/10.1021/acsami.5b02670

6. M.S. Burke, S. Zou, L.J. Enman, J.E. Kellon, C.A. Gabor, E. Pledger, S.W. Boettcher, Revised oxygen evolution reaction activity trends for first-row transition-metal (oxy)hydroxides in alkaline media. J. Phys. Chem. Lett. **6**(18), 3737–3742 (2015). https://doi.org/10.1021/acs.jpclett.5b01650

7. S. Malkhandi, P. Trinh, A.K. Manohar, A. Manivannan, M. Balasubramanian, G.K.S. Prakash, S.R. Narayanan, Design insights for tuning the electrocatalytic activity of perovskite oxides for the oxygen evolution reaction. J. Phys. Chem. C **119**(15), 8004–8013 (2015). https://doi.org/10.1021/jp512722x

8. D. Pletcher, X. Li, S.W.T. Price, A.E. Russell, T. Sönmez, S.J. Thompson, Comparison of the spinels Co3O4 and NiCo2O4 as bifunctional oxygen catalysts in alkaline media. Electrochim. Acta **188**, 286–293 (2016). https://doi.org/10.1016/j.electacta.2015.10.020

9. A.H.A. Monteverde Videla, P. Stelmachowski, G. Ercolino, S. Specchia, Benchmark comparison of Co3O4 spinel-structured oxides with different morphologies for oxygen evolution reaction under alkaline conditions. J. Appl. Electrochem. **47**(3), 295–304 (2017). https://doi.org/10.1007/s10800-016-1040-3

10. K. Fan, H. Chen, Y. Ji, H. Huang, P.M. Claesson, Q. Daniel, B. Philippe, H. Rensmo, F. Li, Y. Luo, L. Sun, Nickel–vanadium monolayer double hydroxide for efficient electrochemical water oxidation. Nat. Commun. **7**, 11981 (2016). https://doi.org/10.1038/ncomms11981

11. O. Diaz-Morales, I. Ledezma-Yanez, M.T.M. Koper, F. Calle-Vallejo, Guidelines for the rational design of Ni-based double hydroxide electrocatalysts for the oxygen evolution reaction. ACS Catal. **5**(9), 5380–5387 (2015). https://doi.org/10.1021/acscatal.5b01638

12. Y. Li, P. Hasin, Y. Wu, NixCo3−xO4 nanowire arrays for electrocatalytic oxygen evolution. Adv. Mater. **22**(17), 1926–1929 (2010). https://doi.org/10.1002/adma.200903896

13. P.W. Menezes, A. Indra, D. Gonzalez-Flores, N.R. Sahraie, I. Zaharieva, M. Schwarze, P. Strasser, H. Dau, M. Driess, High-performance oxygen redox catalysis with multifunctional cobalt oxide nanochains: morphology-dependent activity. ACS Catal. **5**(4), 2017–2027 (2015). https://doi.org/10.1021/cs501724v

14. M. Wiechen, M.M. Najafpour, S.I. Allakhverdiev, L. Spiccia, Water oxidation catalysis by manganese oxides: learning from evolution. Energy Environ. Sci. **7**(7), 2203 (2014). https://doi.org/10.1039/c4ee00681j

15. A. Ramírez, P. Hillebrand, D. Stellmach, M.M. May, P. Bogdanoff, S. Fiechter, Evaluation of MnO_x, Mn_2O_3, and Mn_3O_4 electrodeposited films for the oxygen evolution reaction of water. J. Phys. Chem. C **118**(26), 14073–14081 (2014). https://doi.org/10.1021/jp500939d

16. M. Huynh, C. Shi, S.J.L. Billinge, D.G. Nocera, Nature of activated manganese oxide for oxygen evolution. J. Am. Chem. Soc. **137**(47), 14887–14904 (2015). https://doi.org/10.1021/jacs.5b06382

17. M. Huynh, D.K. Bediako, D.G. Nocera, A functionally stable manganese oxide oxygen evolution catalyst in acid. J. Am. Chem. Soc. **136**(16), 6002–6010 (2014). https://doi.org/10.1021/ja413147e

18. M.M. Najafpour, M. Hołyńska, A.N. Shamkhali, S.H. Kazemi, W. Hillier, E. Amini, M. Ghaemmaghami, D. Jafarian Sedigh, A. Nemati Moghaddam, R. Mohamadi, S. Zaynalpoor, K. Beckmann, The role of nano-sized manganese oxides in the oxygen-evolution reactions by manganese complexes: towards a complete picture. Dalton Trans. **43**(34), 13122–13135 (2014). https://doi.org/10.1039/c4dt01367k

19. P. Hosseini-Benhangi, M.A. Garcia-Contreras, A. Alfantazi, E. Od, L. Gyenge, Method for enhancing the bifunctional activity and durability of oxygen electrodes with mixed oxide electrocatalysts: potential driven intercalation of potassium. J. Electrochem. Soc. **162**(12), 1356–1366 (2015). https://doi.org/10.1149/2.0561512jes.

20. A. Iyer, J. Del-Pilar, C.K. King'Ondu, E. Kissel, H.F. Garces, H. Huang, A.M. El-Sawy, P.K. Dutta, S.L. Suib, Water oxidation catalysis using amorphous manganese oxides, octahedral molecular sieves (OMS-2), and octahedral layered (OL-1) manganese oxide structures. J. Phys. Chem. C **116**(10), 6474–6483 (2012). https://doi.org/10.1021/jp2120737

21. A.C. Thenuwara, S.L. Shumlas, N.H. Attanayake, Y.V. Aulin, I.G. McKendry, Q. Qiao, Y. Zhu, E. Borguet, M.J. Zdilla, D.R. Strongin, Intercalation of cobalt into the interlayer of birnessite improves oxygen evolution catalysis. ACS Catal. **6**(11), 7739–7743 (2016). https://doi.org/10.1021/acscatal.6b01980

22. W. Sun, L.M. Cao, J. Yang, Conversion of inert cryptomelane-type manganese oxide into a highly efficient oxygen evolution catalyst via limited Ir doping. J. Mater. Chem. A **4**(32), 12561–12570 (2016). https://doi.org/10.1039/c6ta03011d

23. P. Legutko, W. Kaspera, P. Stelmachowski, Z. Sojka, A. Kotarba, Boosting the catalytic activity of magnetite in soot oxidation by surface alkali promotion. Catal. Commun. **56**, 139–142 (2014). https://doi.org/10.1016/j.catcom.2014.07.020

24. J. Luo, Q. Zhang, J. Garcia-Martinez, S.L. Suib, Adsorptive and acidic properties, reversible lattice oxygen evolution, and catalytic mechanism of cryptomelane-type manganese oxides as oxidation catalysts. J. Am. Chem. Soc. **130**(10), 3198–3207 (2008). https://doi.org/10.1021/ja077706e

25. I. Atribak, A. Bueno-López, A. García-García, P. Navarro, D. Frías, M. Montes, Catalytic activity for soot combustion of birnessite and cryptomelane. Appl. Catal. B Environ. **93**(3-4), 267–273 (2010). https://doi.org/10.1016/j.apcatb.2009.09.038

26. A. Davo-Quinonero, M. Navlani-Garcia, D. Lozano-Castello, A. Bueno-Lopez, CuO/cryptomelane catalyst for preferential oxidation of CO in the presence of H2: deactivation and regeneration. Catal. Sci. Technol. **6**(14), 5684–5692 (2016). https://doi.org/10.1039/C6CY00329J

27. O.S.G.P. Soares, J.J.M. Órfão, J.L. Figueiredo, M.F.R. Pereira, Oxidation of mixtures of ethyl acetate and butyl acetate over cryptomelane and the effect of water vapor. Environ. Prog. Sustain. Energy **35**(5), 1324–1329 (2016). https://doi.org/10.1002/ep.12348

28. V.P. Santos, S.A.C. Carabineiro, J.J.W. Bakker, O.S.G.P. Soares, X. Chen, M.F.R. Pereira, J.J.M. Órfão, J.L. Figueiredo, J. Gascon, F. Kapteijn, Stabilized gold on cerium-modified cryptomelane: highly active in low-temperature CO oxidation. J. Catal. **309**, 58–65 (2014). https://doi.org/10.1016/j.jcat.2013.08.030

29. V.P. Santos, M.F.R. Pereira, J.J.M. Órfão, J.L. Figueiredo, The role of lattice oxygen on the activity of manganese oxides towards the oxidation of volatile organic compounds. Appl. Catal. B Environ. **99**(1-2), 353–363 (2010). https://doi.org/10.1016/j.apcatb.2010.07.007

30. M.A. Peluso, L.A. Gambaro, E. Pronsato, D. Gazzoli, H.J. Thomas, J.E. Sambeth, Synthesis and catalytic activity of manganese dioxide (type OMS-2) for the abatement of oxygenated VOCs. Catal. Today **133–135**, 487–492 (2008). https://doi.org/10.1016/j.cattod.2007.12.132

31. L. Holmlid, Conditions for forming Rydberg matter: condensation of Rydberg states in the gas phase versus at surfaces. J. Phys. Condens. Matter. **14**(49), 13469–13479 (2002). https://doi.org/10.1088/0953-8984/14/49/305

32. P. Stelmachowski, P. Legutko, T. Jakubek, P. Indyka, Z. Sojka, L. Holmlid, A. Kotarba, Emission of highly excited electronic states of potassium from cryptomelane nanorods. Phys. Chem. Chem. Phys. **17**(39), 26289–26294 (2015). https://doi.org/10.1039/C5CP04108B

33. S. Ching, P.F. Driscoll, K.S. Kieltyka, M.R. Marvel, S.L. Suib, Synthesis of a new hollandite-type manganese oxide with framework and interstitial Cr(III). Chem. Commun. (Camb). **23**(23), 2486–2487 (2001). https://doi.org/10.1039/b107887a

34. A. Kotarba, W. Bieniasz, P. Kuśtrowski, K. Stadnicka, Z. Sojka, Composite ferrite catalyst for ethylbenzene dehydrogenation: enhancement of potassium stability and catalytic performance by phase selective doping. Appl. Catal. A Gen. **407**(1-2), 100–105 (2011). https://doi.org/10.1016/j.apcata.2011.08.029

35. I. Serafin, A. Kotarba, M. Grzywa, Z. Sojka, H. Bińczycka, P. Kuśtrowski, Quenching of potassium loss from styrene catalyst: effect of Cr doping on stabilization of the K2Fe22O34 active phase. J. Catal. **239**(1), 137–144 (2006). https://doi.org/10.1016/j.jcat.2006.01.026

36. M.K. Gulbinska, S.L. Suib, Vanadium-substituted porous manganese oxides with Li-ion intercalation properties. J. Power Sources **196**(4), 2149–2154 (2011). https://doi.org/10.1016/j.jpowsour.2010.10.010

37. E.S. Ilton, J.E. Post, P.J. Heaney, F.T. Ling, S.N. Kerisit, XPS determination of Mn oxidation states in Mn (hydr)oxides. Appl. Surf. Sci. **366**, 475–485 (2016). https://doi.org/10.1016/j.apsusc.2015.12.159

38. T. Jakubek, W. Kaspera, P. Legutko, P. Stelmachowski, A. Kotarba, How to efficiently promote transition metal oxides by alkali towards catalytic soot oxidation. Top. Catal. **59**(10-12), 1083–1089 (2016). https://doi.org/10.1007/s11244-016-0595-x

39. L. Liu, Y. Luo, W. Tan, Y. Zhang, F. Liu, G. Qiu, Facile synthesis of birnessite-type manganese oxide nanoparticles as supercapacitor electrode materials. J. Colloid Interface Sci. **482**, 183–192 (2016). https://doi.org/10.1016/j.jcis.2016.07.077

40. I.R. Leith, M.G. Howden, Temperature-programmed reduction of mixed iron-manganese oxide catalysts in hydrogen and carbon monoxide. Appl. Catal. **37**, 75–92 (1988). https://doi.org/10.1016/S0166-9834(00)80752-6

41. B.S. Yeo, A.T. Bell, Enhanced activity of gold-supported cobalt oxide for the electrochemical evolution of oxygen. J. Am. Chem. Soc. **133**(14), 5587–5593 (2011). https://doi.org/10.1021/ja200559j

42. P. Stelmachowski, A.H.A. Monteverde Videla, K. Ciura, S. Specchia, Oxygen evolution catalysis in alkaline conditions over hard templated nickel-cobalt based spinel oxides. Int. J. Hydrog. Energy **42**(46), 27910–27918 (2017). https://doi.org/10.1016/j.ijhydene.2017.06.034